Influence of nonuniformity in sapphire substrates for a gravitational wave telescope

K. Somiya[*]
Department of Physics, Tokyo Institute of Technology,
2-12-1 Oh-okayama Meguro Tokyo 152-8551, Japan

E. Hirose
Institute for Cosmic Ray Research, the University of Tokyo,
5-1-5 Kashiwa-no-ha, Kashiwa, Chiba 277-8582, Japan

Y. Michimura
Department of Physics, University of Tokyo, Bunkyo, Tokyo 113-0033, Japan

(Received 30 July 2019; published 30 October 2019)

The construction of a large-scale cryogenic gravitational wave telescope, KAGRA, has been completed, and four sapphire test masses have been installed in cryostat vacuum chambers. Recently, it was observed that a sapphire substrate used for one of the input test masses showed a characteristic structure in its transmission map due to nonuniformity of the crystal. We performed an interferometer simulation to observe the influence of the nonuniformity using measured transmission/reflection maps. Shot noise increased by 7% at low frequencies and by 16% at high frequencies. Laser frequency noise coupling increased by 1 order of magnitude. We also found deformation of an alignment control signal and higher tilt coupling in the output optics.

DOI: 10.1103/PhysRevD.100.082005

I. INTRODUCTION

Gravitational waves are ripples of spacetime that carry information of astronomical events from distant galaxies or from the early Universe. Since April 2019, the large-scale telescopes in the United States and Europe (Advanced LIGO [1] and Advanced Virgo [2], respectively) have started the third round of the observation run, and the large-scale cryogenic telescope in Japan, KAGRA [3–5], is to join the observation run from the end of 2019. Whereas the LIGO and Virgo detectors are operated at room temperature with fused silica test masses, KAGRA will be operated in the range 20–23 K with sapphire crystal test masses. Mirror coating thermal noise decreases by a factor of 4 with decreasing temperature and by a factor of 1.3 for a large Young's modulus of sapphire. The material was chosen mainly for three reasons: 1) its high thermal conductivity at cryogenic temperatures, 2) its high mechanical quality factor at cryogenic temperatures, and 3) the high transmittance of the 1064 nm laser, which has been used as a light source in gravitational wave detectors for a few decades. The optical configuration of the telescope consists of a Michelson interferometer with a Fabry-Perot cavity in each arm and two recycling cavities. The four test masses in the arm cavities are sapphire mirrors. The beam splitter and other optics are made of fused silica. We chose the C axis of the sapphire crystal to be perpendicular to the mirror surface to minimize the refractive index variation. We developed a number of sapphire substrates and selected the two with the lowest optical absorption as the input mirrors of the arm cavities [6]. Note that the requirement regarding the substrate absorption imposed on the input mirrors is more severe than that on the end mirrors because the heat absorbed from the incident laser beam in the input mirror substrate can be higher than the heat absorbed in the coatings. As sapphire is not as homogeneous as fused silica, it is essential to correct the transmitted wave front curvature by a technique called ion beam figuring (IBF), in which the physical thickness of the substrate is adjusted point to point so that the wave front error can be within a few nanometers in the clear aperture [7]. After the IBF treatment, however, we found that the measured figure error is larger than the specification (less than 6 nm) by a factor of 4–5, and further, there is a ridgelike structure of height approximately 100 nm in the transmission map, or a so-called transmitted wave front error (TWE) map, of one of the input mirrors. Our mirror team has concluded that this happened because a circular polarization beam was used for measurements in the IBF treatment, which is in fact not reasonable if the substrate is an ideal C-axis crystal. The ridgelike structure would be troublesome because the transmitted beam could contain asymmetric modes as if the

---

[*] somiya@phys.titech.ac.jp

mirror were tilted. It is necessary to find out the influence of this nonuniformity in the TWE map on some control signals and on the sensitivity of the telescope.

The structure of the paper is as follows. In Sec. II, we briefly introduce the interferometer configuration of the KAGRA telescope. In Sec. III, we explain the inhomogeneity of the sapphire substrate and the nonuniformity in our sapphire test masses in greater detail. In Sec. IV, we introduce a modal model interferometer simulation code used for the analysis. In Sec. V, we show some results of the analysis and discuss the influence, namely, i) the increase of shot noise, ii) the increase of laser noise coupling, iii) the deformation of the alignment control signal, and iv) the increase of a tilt noise coupling in the output optics.

II. INTERFEROMETER CONFIGURATION OF KAGRA

Figure 1 shows a schematic of the interferometer. The laser beam with wavelength 1064 nm is first injected to the input mode cleaner to filter out the higher-order spatial modes. The beam is then injected to the input optical isolator, which redirects the beam returning from the interferometer to protect the laser system. The main interferometer is based on a Michelson interferometer with a Fabry-Perot cavity in each arm and two recycling cavities to enhance the circulation power and the bandwidth. The length and the finesse of the arm cavities are 3 km and 1550, respectively. Both the input and end mirrors have a radius of curvature of 1.9 km. The mirror diameter and the thickness are 22 and 15 cm, respectively, and the mass is 23 kg. The wedge angle of the input mirror is 0.025°, and that of the end mirror is 0.05°. The interferometer is operated in a so-called dark fringe, and all the differential fields, including a gravitational wave signal field, reach the antisymmetric port through the output mode cleaner. The arm cavities are, in fact, differentially detuned from the resonance, so a very small fraction of the beam leaks to the antisymmetric port to serve as a reference light of the gravitational wave signal. The output mode cleaner filters out the spatial higher-order modes and radio-frequency control sidebands while transmitting the gravitational wave signal field and the reference beam. All the output mode-cleaner components are mounted on a suspended breadboard, and the relative position and the alignment are controlled using signals from the onboard quadrant photodetectors (QPDs). Additional details regarding the interferometer configuration and the control scheme can be found in Refs. [3,8]. In Sec. V B, we show how much junk light can be found before and after the output mode cleaner. In Secs. V F and V G, we discuss some problems with the output mode-cleaner control related to the TWE maps.

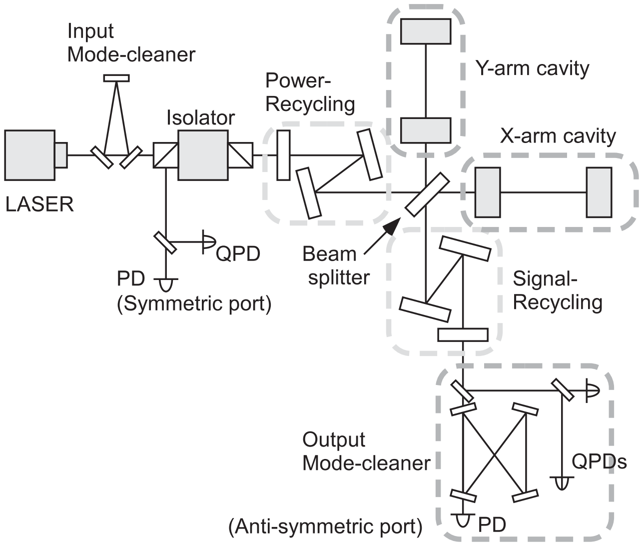

FIG. 1. Rough schematic of the interferometer. Some items that are not mentioned in this paper are omitted, and the photodetectors (PDs) and quadrant photodetectors (QPDs) used in the simulation described in this paper are depicted.

III. INHOMOGENEITY IN THE SAPPHIRE SUBSTRATE

Prior to the procurement of the actual 23 kg sapphire test masses, we asked a vendor to polish a test sample, or the *pathfinder*, and measured the figure error and the inhomogeneity [9]. The diameter and the thickness of the pathfinder were 200 and 60 mm, respectively. The measured rms figure error in the central area (140 mm diameter) was 0.24 nm, which satisfies our requirement of 0.5 nm. The measured inhomogeneity of the pathfinder substrate in terms of the error of the refractive index was $\Delta n = 1.92 \times 10^{-7}$, which corresponds to a TWE of 28.8 nm in a 15 cm thick, 23 kg test mass.

The results of the pathfinder confirm that the IBF treatment is necessary to correct the error in the TWE map. We asked the same vendor to polish the 23 kg sapphire substrates with the IBF treatment for the two substrates that were to be used for the input mirrors (ITMX and ITMY in the x and y arms, respectively). The specification of the rms TWE in the central area (140 mm diameter) was less than 6 nm, and the reported value from the vendor was 3.47 nm for the ITMX and 4.07 nm for the ITMY. However, our independent measurement showed different results: 25.9 nm for the ITMX and 30.1 nm for the ITMY. One difference between the measurements of the vendor and our own measurements is that the vendor used a circular polarization beam and our setup used a linear polarization beam in the Fizeau interferometers. We concluded that the substrate was not perfectly in the C axis and was sensitive to the polarization, thus causing an error in the vendor's measurement, which resulted in the high TWE for either P or S linear polarization after the IBF treatment; the TWE is low for circular polarization.

Figure 2 shows the measured TWE maps of the input mirrors after removing the power term. The beam radius of

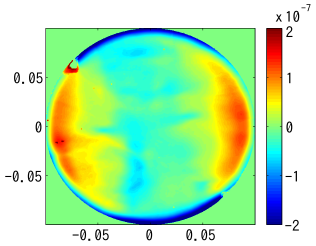

FIG. 2. TWE maps of (left) ITMX and (right) ITMY after removing the power term (curvature), seen from the other side of the high-reflective surface. The plotted area is 20 cm in diameter around the center, and the color bar is in the range ± 20 μm. The rms errors in the central area are 25.9 nm for the ITMX and 30.1 nm for the ITMY.

the input mirrors is 3.5 cm, and therefore the large errors near the edge in the ITMX would not cause too much trouble, while the ridge structure in the ITMY exists near the center and may create a nontrivial coupling between the length motion and the yaw motion.

IV. INTERFEROMETER SIMULATION WITH THE MIRROR MAPS

To investigate the influence of the large TWE of the input mirrors, we need an interferometer simulation with the actual mirror maps. In this study, we use the simulation engine FINESSE, developed by Freise [10]. In the simulation, a light field is decomposed into the orthonormal set of Hermite-Gaussian modes. The amplitude of the beam is given for the mode order (m, n), referring to the x and y directions. In the simulation, the fundamental mode, $(m, n) = (0, 0)$, is defined by the fundamental mode of the input beam or by the mode of the cavity that the beam encounters last, and the beam is extended by the Hermite-Gaussian basis set. The highest order of the Hermite-Gaussian polynomial is set by a user; in our simulation, it is set to $N = 12$. The beam parameter is transformed according to the respective ABCD matrix [11] at each optical component. If a mirror map is implemented in an optical element, the phase and amplitude of the field are calculated in each segment defined in the map. While several types of mirror maps are provided in the FINESSE simulation, we use the reflection map and the transmission (TWE) map, which give the phase shift at the reflection and at the transmission, respectively. The measured TWE maps of the input mirrors have already been shown in Fig. 2. The number of data points is 501×501. The measured reflection maps of the high-reflective (HR) coating of the input mirrors and end mirrors (ETMX and ETMY in the x and y arms, respectively) are shown in Fig. 3. The number of data points is 501×501. Typically, a mirror map has been preprocessed to remove average effects such as a tilt of the entire surface or a curvature error so that the main factors are the surface roughness and the nonuniformity of the refractive index.

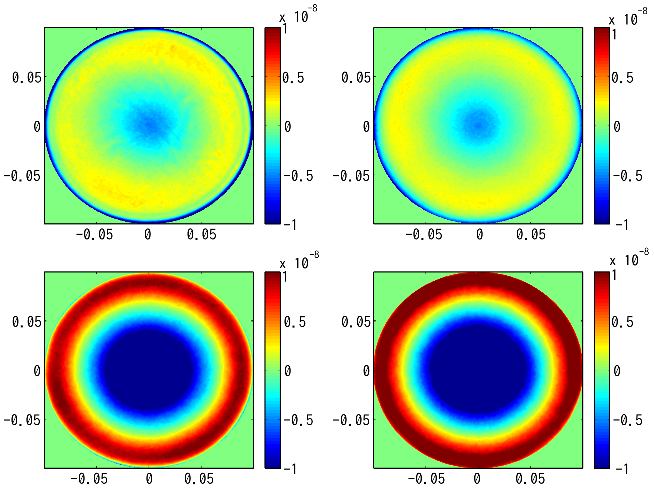

FIG. 3. Phase maps of the HR surface of the (top left) ITMX, (top right) ITMY, (bottom left) ETMX, and (bottom right) ETMY after removing the power term, seen from the HR coating side. The plotted area is 20 cm in diameter around the center, and the color bar range is ± 1 μm for the input mirrors and ± 2 μm for the end mirrors.

The procedure of our simulation is as follows. First, we build up an interferometer with radii of curvature properly determined by analytical calculations. At this moment, no mirror maps are implemented. We then define the cavities so that the mode basis sets are specified. The beam parameters of the input beam are given accordingly, and they will not be changed afterward. Then, we replace the radii of curvature by the measured values and implement the mirror maps. We also include an aperture with 20 cm in diameter on each test mass. A mirror map causes a slight change in the average position of the reflection surface for the fundamental mode beam, and this change is modified manually. There are seven steps to be performed:

(i) To tune the position of the end mirror in each arm, we probe the transmitted beam to find the maximum transmitted power with regard to the microscopic cavity length, or, in other words, the phase of the end mirror. For this simulation, the recycling cavities have be turned off, not only to set the reflectivities of the recycling mirrors to zero but also to stop defining the recycling cavities.

(ii) Once the end mirror positions are tuned, the next parameter to be tuned is the beam splitter position. This is necessary even though we do not implement the beam splitter map in this study. We probe the amplitude of the fundamental mode at the antisymmetric port and find the minimum amplitude with regard to the phase of the beam splitter. Note that the output mode cleaner is removed at this point.

(iii) Resetting the reflectivities of the recycling mirrors, we probe the transmitted beam of the end mirror of the x-arm cavity to find the maximum with regard to the power-recycling mirror phase.

(iv) To tune the phase of the signal-recycling mirror, a signal field has to be generated. In our simulation, a differential signal is generated at 10 kHz. We probe the amplitude of the signal field at the antisymmetric port without the output mode cleaner and find the maximum with regard to the signal-recycling mirror phase. In this study, we assume a nondetuned signal recycling cavity, which will be the configuration of KAGRA in the first observation run. If a simulation with the detuned signal-recycling cavity is required, the detuned angle should be added to the phase of the signal recycling mirror after this tuning process.

(v) Though not depicted in Fig. 1, there are two curved mirrors before the output mode cleaner to mode match the beam from the interferometer to the output mode cleaner. We probe the amplitude of the 10 kHz signal field at the antisymmetric port with the output mode cleaner and find the maximum with regard to the distance of the two mode-matching telescope mirrors. In fact, this step is skipped for this study because we do not plan to move the curved mirrors for the mode matching during the first observation run.

(vi) Now, we have to determine the amount of the offset for the reference beam to extract the gravitational wave signal. The reference light consists of the component due to the imbalance of the reflectivities of the arm cavities and the component due to an intentional offset of the arm cavity lengths. Although we plan to optimize the balance of these two components in the final stage of the KAGRA operation [3], the offset component will be set much larger than the imbalance component during the first observation run. The phase of each arm cavity being finely tuned after process i, the reflectivity imbalance component, which is sometimes called the contrast defect, is the only fundamental mode carrier light at the antisymmetric port. To tune the balance between the two components, we measure the power of the contrast defect and then determine the amount of offset. If we wish the reference light to be mostly the offset component, the amount of the offset is determined to make the total light power at the antisymmetric port approximately 40 mW. In this study, we have chosen the latter setup.

(vii) The last step is to align the beam into the output mode cleaner. This step would not be necessary if the mirror map did not have an asymmetric structure that imparts a virtual tilt to the reflected/transmitted beam. Indeed, the beam was already centered with respect to the output mode cleaner in our previous studies with artificial mirror maps [12,13]. Instead of tilting the four-mirror bow tie cavity simultaneously in the FINESSE simulation, we tilt the pair of steering mirrors before the output mode cleaner to maximize the transmission of the signal field. Table I shows a list of the major interferometer parameters.

TABLE I. Some interferometer parameters used in the simulation. The radii of curvature (RoC) of the test masses are the ones measured [6]. The reflectivities of the test masses are given with an assumption of 10% imbalance in the optical loss and 0.5% imbalance in the finesse. Here, BS stands for beam splitter, PRM stands for power-recycling mirror, SRM stands for signal-recycling mirror, OMMT stands for output mode-matching telescope, and OMC stands for output mode cleaner.

Parameter	Value
Laser power	55.375 W
Control sideband frequencies	16.88 MHz/45.01 MHz
BS-ITMX distance	26.6649 m
BS-ITMY distance	23.3351 m
Recycling-cavity length	66.59 m
ITMX/Y RoC	1904.6 m/1904.4 m
ETMX/Y RoC	1908.24 m/1905.55 m
ITMX/Y reflectivities	99.602%/99.598%
ETMX/Y reflectivities	99.9941%/99.9949%
PRM/SRM reflectivity	90%/70%
OMMT mirrors RoC	13.16 m/44.39 m
OMC Gouy phase	55.4 deg
OMC finesse	780

V. RESULTS

A. Parameters after tuning

As mentioned in Sec. IV, the phases of some mirrors have to be tuned after implementing mirror maps. We performed two simulations: one with only the HR maps of the test masses and the other with the HR maps and the TWE maps of the input mirrors. Table II shows the mirror phases after the tuning process. The output mode-matching telescope length was not changed after the tuning with the mirror maps. The output mode-cleaner tilt and centering did not change much with the HR maps. They did not change much even with the TWE maps in the vertical direction (y direction).

TABLE II. Mirror phases after the tuning with the HR maps only and with the HR + TWE maps. See the caption of Table I for the abbreviations.

	No map	HR only	HR + TWE
ETMX phase (deg)	90.0012	96.3419	96.3420
ETMY phase (deg)	−0.0012	6.9570	6.9569
BS phase (deg)	0	0.2098	8.5733
PRM phase (deg)	0	0.4604	8.9757
SRM phase (deg)	0	−0.9631	2.0147
OMMT length (m)	2.6	2.6	2.6
OMC x-tilt (rad)	0	-12μ	-96μ
OMC x-centering (m)	0	7μ	13μ
OMC y-tilt (rad)	0	0μ	-4μ
OMC y-centering (m)	0	0μ	0μ

B. Higher-order modes at the antisymmetric port

Figure 4 shows the beam images immediately after the signal-recycling mirror. The color bar shows the intensity in watts per square meter. The control sideband fields are removed. The fundamental mode carrier beam is not removed. One can see that the TWE maps have made the beam dirty; in other words, more spatial higher-order modes are mixed in the fundamental mode.

The output mode cleaner can filter out the higher-order modes to some extent. Table III shows the power of each mode before and after the output mode cleaner in the case with and without the input mirror TWE maps. Note that we neglected the optical losses and surface distortion in the output mode cleaner. The contribution of the optical loss in the actual output mode-cleaner transmission is estimated to be approximately 2%. One can see that the higher-order modes increased with the TWE maps by 1 or 2 orders of magnitude. The total power of the higher-order modes after the output mode cleaner is 0.11 μW without the TWE and 1.82 μW with the TWE; it is 16 times more with the TWE but is as low as 40 ppm of the reference light thanks to the high-finesse output mode cleaner.

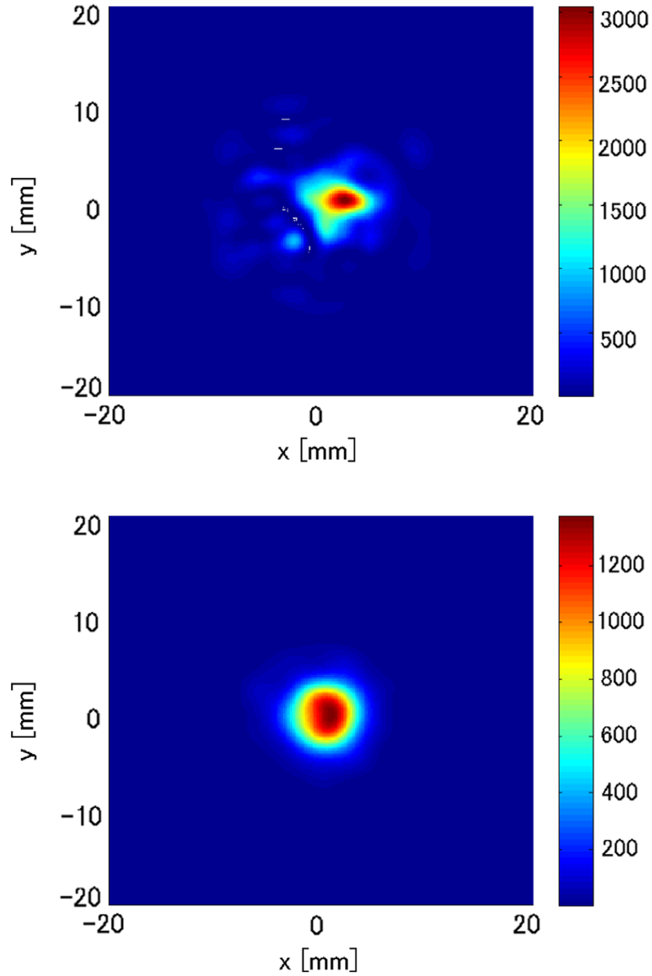

FIG. 4. Images of the beam right after the signal-recycling mirror with and without the input mirror substrate transmitted wave front error (*top* and *bottom*, respectively).

TABLE III. Power of nth-order modes ($n = 0, 1, 2, \ldots, 12$) before and after the output mode cleaner with and without the TWE maps.

	HR only (W)		HR + TWE (W)	
n	Before OMC	After OMC	Before OMC	After OMC
0	4.3e-2	4.0e-2	4.3e-2	4.7e-2
1	1.7e-3	6.2e-9	1.8e-2	2.3e-8
2	1.1e-3	2.4e-9	1.1e-2	3.6e-8
3	4.0e-4	2.7e-8	4.7e-3	3.0e-7
4	4.8e-4	3.6e-9	6.0e-3	7.9e-8
5	2.2e-5	9.6e-11	3.8e-3	2.1e-8
6	5.7e-5	1.4e-9	5.5e-3	1.4e-7
7	1.6e-4	2.9e-9	1.4e-3	2.8e-8
8	1.0e-4	8.3e-10	1.0e-2	4.1e-8
9	1.9e-4	1.2e-9	1.3e-2	1.1e-7
10	8.4e-4	3.5e-8	2.3e-2	6.3e-7
11	1.1e-3	2.7e-8	3.1e-2	3.2e-7
12	8.5e-4	5.2e-9	2.0e-2	7.7e-8

Here, the fundamental mode beam is not exactly 40 mW in some cases. This is because step vii was taken after tuning the offset. The output mode-cleaner cavity mode was redefined, and the fundamental mode increased.

C. Shot noise–limited sensitivity

An increase in shot noise due to the higher-order modes will be approximately 0.7% or less with the approximately 40 mW reference light. If the reference light power is reduced to approximately 10 mW, the contribution will be 1.3%.

A larger concern is a possible decrease in the signal field after the output mode cleaner. If the wave front of the signal field is distorted by the transmission error of the input mirrors in a nonspherical way, a fraction of the signal field beam will have to be filtered by the output mode cleaner. (In fact, because we skipped step iv, even a spherical distortion cannot be compensated by tuning the output mode-matching telescope in this study.) We performed a simulation to calculate the signal field amplitude of each mode, and the contribution of the higher-order modes to the total signal field at the antisymmetric port was 0.08% with the HR maps only and 4.5% with the HR + TWE maps.

Another concern is a possible decrease in the power-recycling gain. We performed a simulation to compare the power-recycling gain of the fundamental mode, and it was 9.4 with the HR maps only and 8.5 with the HR + TWE maps. Note that we do not assume any optical losses in the power-recycling mirror or in the beam splitter.

Figure 5 shows the shot noise–limited sensitivities with the HR maps only and with the HR + TWE maps. The shot noise level is 7.1% worse at low frequencies and 16% worse at high frequencies with the TWE maps.

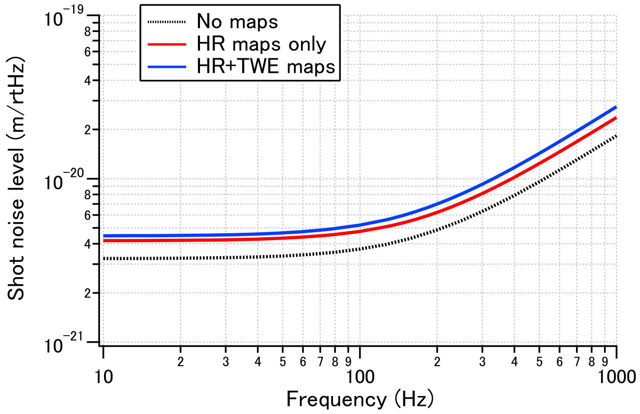

FIG. 5. Shot noise–limited sensitivities with the HR maps only and with the HR + TWE maps.

D. Laser noise coupling

All the second-generation gravitational wave telescopes including KAGRA employ the homodyne readout scheme, in which a reference beam is sent at the carrier frequency to the antisymmetric port, and a beat note is taken with the signal field. This is an updated readout scheme compared to the conventional heterodyne readout scheme, in which the input field is modulated by a radio frequency and a beat note of this sideband field and the signal field is taken at the antisymmetric port. One advantage of the homodyne readout scheme is that the reference beam, mainly generated with a differential offset to the arm length, experiences both a low-pass filter of the arm cavity and a low-pass filter of the power-recycling cavity to suppress laser noise coupling [14]. If the reference beam is not generated in the arm cavities but in the central interferometer, the second low-pass filter will be eliminated, and the laser noise contribution will increase. We perform a simulation to investigate the laser noise coupling with the substrate's nonuniformity. Figure 6 shows the result. One can see that the laser frequency noise coupling increases with the TWE maps by more than 1 order of magnitude in the observation frequency band.

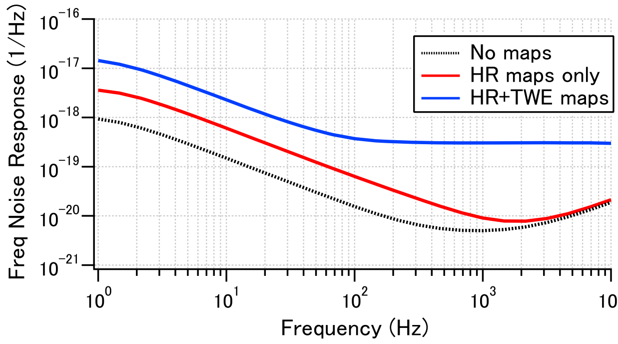

FIG. 6. Laser noise couplings with and without the TWE maps.

E. Wave front–sensing signal

A possible distortion of a control signal is another type of concern with this kind of structure in the transmissive optics. We calculated the wave front–sensing signal of the common-mode tilt of the arm cavities obtained at the symmetric port. Wave front sensing is a well-established method to probe a small tilt of the optics in a cavity [15]. A TEM10 or TEM01 mode of the probe beam in a cavity couples with a reference beam, which is usually a radio-frequency sideband field that does not enter the cavity, to be detected at a pair of QPDs. The tilts of the cavity optics can be decomposed into a symmetric (hard) mode and an antisymmetric (soft) mode. Each mode of the two arm cavities makes common and differential modes. The Gouy phases of the beam at the two QPDs are appropriately chosen to minimize the cross-coupling of the signals.

Figure 7 shows the wave front–sensing signals with regard to the common-hard mode tilt, as an example. Compared with the case without the TWE maps, the wave front–sensing signal in the *x* direction is deformed, and the zero-crossing point is offset with the TWE maps.

F. Alignment control of the output mode cleaner

The alignment control signal of the output mode cleaner is obtained from the photodetector (PD) at the transmission of the cavity and from the QPDs at the pickoff before the cavity. The former is for fine alignment, and the latter is for a course alignment. All the PDs are mounted on a

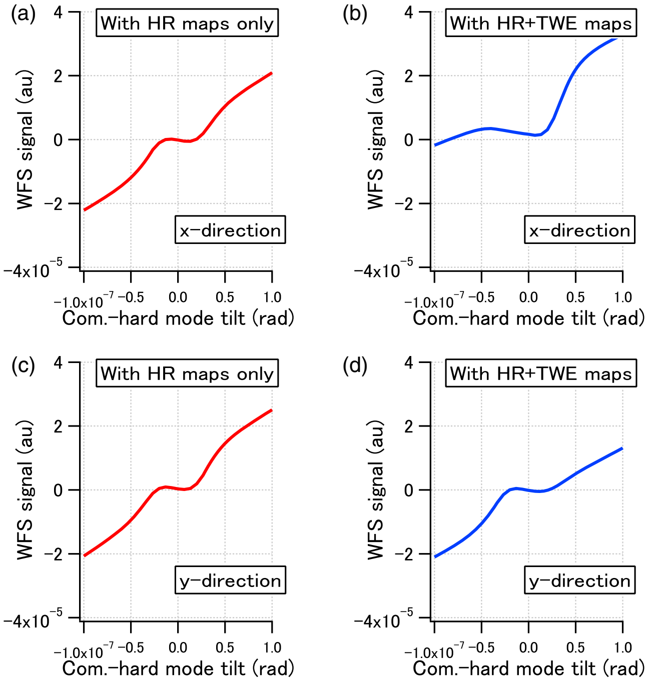

FIG. 7. Wave front–sensing signals (a) in the *x* direction with the HR maps only, (b) in the *x* direction with the HR + TWE maps, (c) in the *y* direction with the HR maps only, and (d) in the *y* direction with the HR + TWE maps.

TABLE IV. Sensing matrices of the alignment control of the output mode cleaner with and without the TWE maps.

HR only		
	x-misc	x-tilt
QPD1	−9.7 W/m	−1.0 W/rad
QPD2	8.0 W/m	4.5 W/rad
	y-misc	y-tilt
QPD1	−9.8 W/m	1.0 W/rad
QPD2	−8.1 W/m	4.6 W/rad

HR + TWE		
	x-misc	x-tilt
QPD1	−8.3 W/m	−1.9 W/rad
QPD2	6.0 W/m	4.3 W/rad
	y-misc	y-tilt
QPD1	−7.6 W/m	1.3 W/rad
QPD2	−7.3 W/m	4.4 W/rad

semimonolithic breadboard for the output mode cleaner so the QPDs can probe the relative tilt and miscentering of the beam with respect to the output mode-cleaner cavity. The QPDs are approximately 46 cm distant where the Rayleigh range is approximately 56 cm.

Table IV shows the sensing matrices of the alignment control of the output mode cleaner. Two QPDs probe the tilt and miscentering. The control signals can be obtained separately as long as the responses to the 2 degrees of freedom (DOF) are somewhat independent. According to Ref. [16], the sensing noise level of a 2 DOF system with a sensing matrix $((a,b),(c,d))$ is given by

$$\langle x_1\rangle = \frac{1}{1-\eta}\left(\frac{\langle n_1\rangle}{a} + \eta\frac{\langle n_2\rangle}{c}\right),$$

$$\langle x_2\rangle = \frac{1}{1-\eta}\left(\frac{\langle n_2\rangle}{d} + \eta\frac{\langle n_1\rangle}{b}\right),$$

with the degeneracy factor $\eta \equiv bc/ad$. In our case, $\langle x_1\rangle$ and $\langle x_2\rangle$ are the miscentering sensing noise and the tilt sensing noise, respectively; the bracket denotes the ensemble average. Here, $\langle n_j\rangle$ is the noise in a PD, which is proportional to the square root of the light power at a PD and hence almost the same with or without the TWE maps. For effective tilt/miscentering sensing with two QPDs, the distance of the QPDs is set far enough compared with the Rayleigh range, and the degeneracy factor η is far from unity without the TWE maps: 0.18 for the miscentering and 0.18 for the tilt sensing. With the TWE maps included, however, the degeneracy factor becomes 0.32 for the miscentering and 0.28 for the tilt sensing.

G. Tilt coupling at the output mode cleaner

Through a design study of KAGRA's output mode cleaner, we have found that an asymmetric structure in a transmissive object imposes a more severe requirement on the seismic isolation system of the output mode cleaner. As explained in Sec. V D, a reference light is needed to extract a gravitational wave signal. A tilt or miscentering of the output mode cleaner generates an amplitude modulation on the reference light, converting the fundamental mode into first-order Hermite-Gaussian modes. This effect could be, however, quadratic to the tilt or miscentering, if the cavity is aligned to the reference light well. Incidentally, the tilt or miscentering also reduces the gravitational wave signal transmitted through the output mode cleaner. This effect could also be quadratic to the tilt or miscentering. In fact, the optimal alignment to maximize the signal transmission is different from that to minimize the conversion of the reference light if one of the transmissive objects has an asymmetric structure.

Figure 8 shows how much the reference light power changes with the tilt and miscentering of the output mode

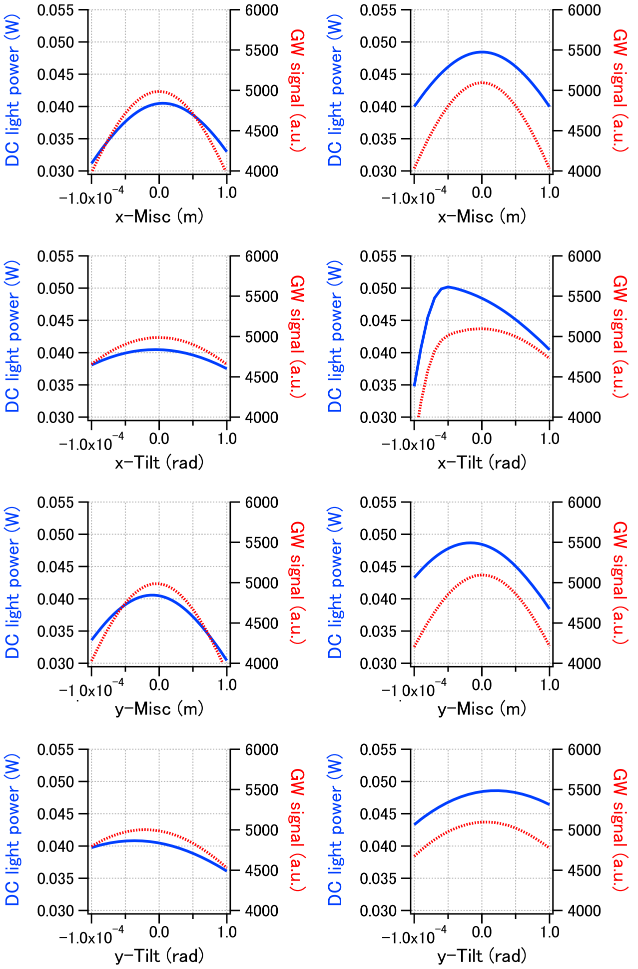

FIG. 8. Power of reference dc light power (solid curve) and the gravitational wave signal field (dashed curve) transmitted through the output mode cleaner with respect to the tilt and miscentering of the output mode cleaner in the x and y directions. *Left*: With HR maps only. *Right*: With HR + TWE maps.

TABLE V. Summary of the results. Here, FN stands for frequency noise, ASC stands for alignment sensing control, and OMC stands for the output mode cleaner. The OMC ASC and the OMC tilt coupling are for the *x* direction. Those for the *y* direction do not show a significant increase with the TWE maps.

Parameter	No map	HR only	HR + TWE
Power-recycling gain	16.7	9.4	8.5
Shot noise at 100 Hz ($\mathrm{m}/\sqrt{\mathrm{Hz}}$)	3.7e-21	4.6e-21	5.2e-21
FN response at 100 Hz (1/Hz)	1.6e-20	6.3e-20	3.7e-19
FN response at 1 kHz (1/Hz)	5.0e-21	9.1e-21	3.0e-19
Wave front sensing		(see Fig. 7)	
OMC ASC degeneracy	7%	18%	32%
OMC tilt coupling (W/rad)	0.0	3.2	50

cleaner. With the HR maps only, the reference light power mostly peaks at the operation point where the signal transmission is maximized. With the TWE maps included, however, the reference light peaks at a different point for the tilt in the *x* direction. The response to the tilt in the *x* direction at the operation point is calculated to be 52 W/rad. It is 16 times larger than that in the *x* direction with the HR maps only. The response to the tilt is not as good in the *y* direction even with the HR maps only, 20 W/rad, but the response in the *x* direction with the TWE maps is even worse. A large response imposes a severe requirement on the seismic isolation system of the output mode cleaner.

VI. CONCLUSIONS

In this paper, we performed a number of simulations with measured mirror maps to investigate the influence of the nonuniformity in the sapphire substrate used as an input mirror of KAGRA. First, we calculated the amount of the spatial higher-order modes at the antisymmetric port and found that the total amount of the higher-order modes power is 16 times larger with the transmission maps. It was observed that 4.5% of the signal field is scattered to the higher-order modes with the TWE maps, whereas it is 0.08% with the HR maps only. We also found that the power-recycling gain was reduced from 9.4 to 8.5. As a result, the shot noise level increased by 7.1% at low frequencies and by 16% at high frequencies. The laser frequency noise level increased by more than 1 order of magnitude in the observation band. The wave front–sensing signal of the common hard mode is deformed, especially in the *x* direction with the TWE maps. The degeneracy of the output mode-cleaner alignment sensing matrix increases by a factor of 1.5–2. Finally, we found that the output mode-cleaner tilt noise coupling in the *x* direction increases with the TWE maps. It is 2.6 times larger than that in the *y* direction with the HR maps only, which is the largest value before introducing the TWE maps. Table V summarizes all the results.

Among all the problems, the most serious problem would be the laser noise coupling. According to Ref. [14], there is a safety margin of a few orders of magnitude between the frequency noise–limited sensitivity and the quantum noise–limited sensitivity of the broadband configuration. We assume, however, a 0.5% imbalance in the arm cavity finesse and losses. A recent measurement of the input mirror reflectivity has revealed a larger (approximately 10%) imbalance due to a nonsimultaneous coating production. This additional factor of 20 would bring frequency noise quite close to degrade the sensitivity of KAGRA. A further investigation with the latest parameters is required.

It has been reported from the LIGO group that a point defect in one of the silica substrates locally increases the temperature due to heat absorption from the laser and causes a wave front distortion [17]. This phenomenon is analogous to the nonuniformity of the sapphire substrate in KAGRA. The LIGO researchers have decided to displace the beam from the center of the mirror so that the heat absorption at the point defect decreases. KAGRA could attempt this, but the effect would be smaller because our structure in the TWE map exists even if the laser power is reduced. A further investigation using the modal model simulation is required to see how much improvement can be expected in KAGRA with the intentional miscentering of the beam.

This paper demonstrates the use of modal model simulation to investigate the influence of some defects on a gravitational wave telescope. This type of simulation is a powerful tool that enables the instrument to be designed before the actual start of an observation and also allows the characterization of the observed phenomena when the instruments are commissioned during the observation run.

ACKNOWLEDGMENTS

This work was supported by MEXT, JSPS Leading-edge Research Infrastructure Program, JSPS Grant-in-Aid for Specially Promoted Research 26000005, JSPS Grant-in-Aid for Scientific Research on Innovative Areas 2905 (Grants No. JP17H06358, No. JP17H06361, and No. JP17H06364), JSPS Core-to-Core Program A. Advanced Research Networks, the joint research program of the Institute for Cosmic Ray Research, University of

Tokyo, and the Mitsubishi Foundation. This research activity has also been supported by the European Commission within the Seventh Framework Programme (FP7)-Project ELiTES (Grant Agreement No. 295153). The authors would like to especially thank Hiro Yamamoto at Caltech for valuable discussions. They would like to thank Editage (http://www.editage.com) for editing and reviewing this manuscript for the English language.

[1] B. P. Abbott *et al.*, Phys. Rev. Lett. **116**, 061102 (2016).

[2] Virgo Collaboration, Advanced Virgo baseline design, VIR-0027A-09, 2009, https://pub3.ego-gw.it/itf/tds/.

[3] K. Somiya (KAGRA Collaboration), Classical Quantum Gravity **29**, 124007 (2012).

[4] T. Akutsu *et al.*, Prog. Theor. Exp. Phys. **2018**, 013F01 (2018).

[5] T. Akutsu *et al.*, Classical Quantum Gravity **36**, 165008 (2019).

[6] E. Hirose *et al.* (to be published).

[7] https://www.zygo.com/.

[8] Y. Aso, Y. Michimura, K. Somiya, M. Ando, O. Miyakawa, T. Sekiguchi, D. Tatsumi, and H. Yamamoto (The KAGRA Collaboration), Phys. Rev. D **88**, 043007 (2013).

[9] E. Hirose, D. Bajuk, G. Billingsley, T. Kajita, B. Kestner, N. Mio, M. Ohashi, B. Reichman, H. Yamamoto, and L. Zhang, Phys. Rev. D **89**, 062003 (2014).

[10] A. Freise, D. Brown, and C. Bond, arXiv:1306.2973.

[11] A. E. Siegman, *Lasers* (University Science Books, Sausalito, CA, 1986).

[12] A. Kumeta, C. Bond, and K. Somiya, Opt. Rev. **22**, 149 (2015).

[13] K. Yano, A. Kumeta, and K. Somiya, J. Phys. Conf. Ser. **716**, 012032 (2016).

[14] K. Somiya, Y. Chen, S. Kawamura, and N. Mio, Phys. Rev. D **73**, 122005 (2006).

[15] D. Z. Anderson, Appl. Opt. **23**, 2944 (1984).

[16] K. Somiya and O. Miyakawa, Appl. Opt. **49**, 4335 (2010).

[17] A. Brooks *et al.*, The point absorbers, *LVC Meeting March 2019* (USA, 2019), LIGO-DCC-G1900203-v5.